ENG. Struct. Civ. Eng. 2026, 20(4): 869–891
https://doi.org/10.1007/s11709-026-1304-x

RESEARCH ARTICLE

Mechanical properties of magnesium phosphate cement-based ultra-high-performance concrete prepared at negative temperatures: A prediction model based on adaptive weighted stacking

Xin HUANG[a], Xin CHEN[b], Jie YUAN[a*], Junbo WANG[a], Yang LIU[a*]

[a] *School of Transportation Science and Engineering, Harbin Institute of Technology, Harbin 150090, China*
[b] *College of Field Engineering, Army Engineering University of PLA, Nanjing 210007, China*
[*] *Corresponding authors. E-mails: hityuanj@163.com; ly7628@hit.edu.cn*

ABSTRACT Magnesium phosphate cement-based ultra-high-performance concrete (MPC-UHPC), which is characterized by rapid hardening and high early strength, is recognized as an ideal material for the post-disaster reconstruction and wartime emergency repair of critical infrastructure in cold regions. However, laboratory conditions are frequently inadequate for accurately simulating natural severe cold environments, which can lead to deviations in the development of the mechanical properties of MPC-UHPC from anticipated performance, thereby increasing the time and cost associated with trial mix designs. In this study, an adaptive weighted stacking model was proposed, which quantifies the prediction errors of base learners. This model achieved a coefficient of determination of 0.917 and 0.935 for predicting the flexural and compressive strength of MPC-UHPC at negative temperatures, respectively, significantly outperforming any single model. Steel fiber content and ambient temperature were identified as the dominant factors influencing the flexural and compressive strength, respectively. Shapley additive explanations analysis further indicated that a low water-to-cement ratio, high V_f, and low borax-to-MgO ratio are essential for achieving optimal mechanical properties at negative temperatures; however, these parameters must be adjusted while ensuring acceptable workability. This study provides a reliable quantitative tool for predicting the mechanical properties of MPC-UHPC in severely cold regions, which serves as a powerful guide for optimizing mix proportions with respect to hardened-state performance.

KEYWORDS magnesium phosphate cement, ultra-high-performance concrete, machine learning, mechanical properties prediction, negative temperature

1 Introduction

Ultra-high-performance concrete (UHPC) is a fiber-reinforced composite with outstanding mechanical properties and durability [1]. Commercially available UHPC generally utilizes Portland cement modified with mineral additions as the cementitious material. When used for construction at negative temperatures in winter, it requires additional thermal insulation curing measures, which fail to meet the demands for emergency repair and construction. For UHPC projects exposed to low ambient temperatures, subjected to tight construction schedules, and lacking convenient curing conditions, Portland cement should be replaced with a special type of cement that exhibits rapid setting and high early strength. Among such special cements, magnesium phosphate cement (MPC) has the lowest activation energy of reaction [2], thereby exhibiting the greatest potential for application under negative temperatures, with demonstrated use in emergency repairs of roads and airport pavements in cold regions [3,4]. The concept of MPC-UHPC was first proposed by Qin et al. [5] in 2022, with compressive strengths (*CS*s) exceeding 150 MPa under ambient curing conditions [6,7]. Subsequently, Yuan et al. [8] developed

Article history: Received Sep 5, 2025; Accepted Jan 4, 2026

an MPC-UHPC adaptable to sub-zero environments by partially replacing dead-burnt MgO (DBM) with light-burnt MgO (LBM) and fly ash microspheres, a method that enhanced the system's reactivity while maintaining adequate workability. This MPC-UHPC, when cured at a constant –10 °C, was reported to achieve a *CS* exceeding 120 MPa after 28 d. Furthermore, it could withstand over 600 rapid freeze–thaw cycles and was projected to have a safe service life of more than 100 years in saliferous and severely cold environments. However, limited by their experimental conditions, Yuan et al. [8] adopted some mix proportion parameters based on empirical values for normal-temperature MPC-UHPC or determined them through a process of selection at ambient temperatures, followed by verification in sub-zero environments. This approach could not guarantee that all the obtained parameters were optimal for the target cold-weather conditions.

As publications on MPC-based materials and UHPC continue to increase, data-driven mix proportion design methods, which differ from mechanism-driven approaches, have garnered growing attention. Hou et al. [9] utilized the response surface method to develop a suitable equation for predicting the early-age *CS* of MPC paste based on the MgO-to-phosphate ratio (*M*/*P*), water-to-cement ratio (*W*/*C*), and borax-to-MgO ratio (*B*/*M*). However, traditional regression models exhibit limitations in fitting accuracy when handling nonlinear relationships between multiple interacting parameters and macroscopic performance [10]. In recent years, machine learning (ML) has been increasingly applied in the field of cement-based composite design. Compared to traditional empirical formulas, ML prediction models offer greater speed and higher accuracy in predicting the performance of cement-based composites [11,12]. Initially, research primarily focused on single prediction models. According to Sadrossadat et al. [13], the use of an artificial neural network (ANN) model yielded a 20% lower prediction error for UHPC slump than traditional approaches, including multiple linear regression (LR) and the response surface methodology. Yu et al. [14] predicted the *CS* of high-performance concrete (HPC) using a support vector regression (SVR) model, achieving a coefficient of determination (R^2) value of 0.94. However, the selection of kernel functions in SVR algorithms largely depends on repeated trial and error, and both computational cost and time increase sharply as the data set size grows. Both SVR and ANN algorithms suffer from limited transparency in their opaque mechanisms and poor interpretability [15,16]. Furthermore, most single prediction models are prone to issues such as underfitting or insufficient generalization ability when handling complex, nonlinear prediction tasks [17]. Consequently, ensemble models have been proposed to integrate the performance advantages of multiple models via fusion strategies (bagging or boosting) [18], significantly improving the accuracy of prediction models [19]. Khan et al. [20] compared the performance of algorithms such as *k*-nearest neighbors, random forest (RF), SVR, and extreme gradient boosting (XGB) in constructing a prediction model for the *CS* of UHPC and found that the ensemble model XGB achieved significantly higher predictive accuracy than the other three single models. Prediction models for the *CS* of magnesium potassium phosphate cement mortar were developed by Ma et al. [21] using ANN (single model) and XGB (ensemble model). The effects of different mineral additions on the *CS* were systematically evaluated. The ensemble model XGB was demonstrated to exhibit superior learning capability, achieving a predictive accuracy of 0.926 (R^2).

Zhang et al. [22] combined two phosphate systems, ammonium dihydrogen phosphate (ADP) and potassium dihydrogen phosphate (KDP), to create a data set with 18 input features, and established a *CS* prediction model for MPC concrete, respectively, using an improved single algorithm, particle swarm optimization of back propagation ANN, and an ensemble algorithm (RF). The findings indicated that the single model required hyperparameter optimization to match the predictive accuracy of the ensemble model, and that the primary factors influencing *CS*, ranked by importance, were curing age, MgO purity, *M*/*P*, and *W*/*C*. Although ensemble models generally provide higher predictive accuracy than single models, standard ensemble methods combine base learners according to relatively simple predefined rules. For example, bagging is implemented through averaging in regression tasks or voting in classification tasks, while boosting trains base learners sequentially and combines them by adjusting weights dynamically based on the prediction errors from the previous iteration. However, such fixed ensemble strategies cannot model the complex nonlinear dependencies among the prediction outputs of base learners [23]. To overcome this limitation and further improve predictive accuracy, the stacking ensemble algorithm has been proposed, which redefines the ensemble process of base learners as a learning problem. In this approach, the prediction results of multiple base learners are treated as new meta-features, on which a meta-learner is trained to generate the final prediction [24]. A stacking model was constructed by Li and Wang [25] to predict the *CS* of HPC using XGB, RF, gradient boosting decision tree (GBDT), and categorical boosting (CB). Compared with the XGB and SVR models, the stacking model achieved R^2 values that were higher by 2% and 32%, respectively, while its mean squared error (*MSE*) was reduced by 51% and 92%, respectively. However, the stacking ensemble learning has not yet been applied to the design and prediction of MPC-based materials.

This study aims to develop a highly accurate prediction model for the mechanical properties of MPC-UHPC at negative temperatures, identify the influence patterns of input features on these properties, and propose recommended ranges for key mix proportion parameters. A database of MPC-UHPC mechanical properties at negative temperatures was established by compiling data from relevant literature, with each source rigorously assigned a group ID to ensure methodologically sound, leakage-free validation. Twelve mainstream ML models were evaluated, from which four optimal base learners were selected, and their hyperparameters were optimized. Ultimately, an adaptive weighted stacking (AW-stacking) model was constructed, in which weights were adaptively assigned to each base learner according to their prediction errors, with Bayesian regression employed as the meta-learner. To achieve a closed-loop model lifecycle, Shapley additive explanations (SHAP)-based interpretability analysis was applied to elucidate the influence patterns of input features on the prediction model, and a graphical user interface (GUI) was developed to enable visualization and interactive demonstration of the model. The research workflow is presented in Fig. 1.

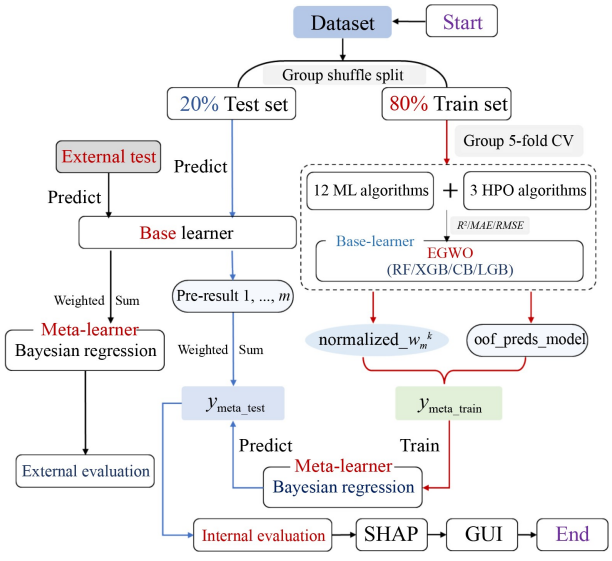

Fig. 1 Research flowsheet.

2 Data set establishment

Compared with normal-temperature conditions, the mechanical properties of MPC-UHPC at negative temperatures are influenced by a broader range of factors. For example: 1) the testing temperature is typically maintained at 20 °C under normal-temperature conditions. A decrease in environmental temperature can retard the hydration rate of MPC, degrade the morphology of struvite, and alter the pore structure distribution [26], thereby affecting its macroscopic performance; 2) the use of LBM is generally avoided at normal-temperature conditions to prevent excessively rapid setting and hardening of MPC. However, under negative temperatures, LBM can enhance the activity of the reaction system and promote the continuous hydration of MPC [3]; 3) using crushed ice or snow instead of mixing water is an effective technique for improving efficiency in emergency repair projects [27]; 4) molds made of different materials have distinct thermal conductivities. Under negative temperatures, the thermal conductivity of molds impacts the rate at which heat is dissipated following casting, thereby influencing the early hydration process of MPC-UHPC [8].

Based on the above considerations, ten basic input features were included in this study: *M*/*P*, *W*/*C*, *B*/*M*, sand-to-binder ratio (*S*/*B*), fly ash content (*FA*), silica fume content (*SF*), steel fiber content (V_f), curing age (age), length-to-diameter ratio (*L*/*D*), and types of phosphate (*XDP*). Additionally, four extra input features were considered: ambient temperature (*T*), LBM-to-DBM ratio (*LBM*/*M*), types of mixing water (*W*), and types of mold material (Mold). The *XDP* comprised ADP and KDP. *W* was partitioned into water and crushed ice, whereas Mold was categorized as either a plastic mold or a steel mold. The output variables included flexural strength (*FS*) and *CS*.

2.1 Data collection and processing

A database of MPC-UHPC negative temperature mechanical properties was established based on Refs. [3–8,27–44]. The summary of data sources is listed in Table A1 in Appendix. Furthermore, data from Refs. [4,44] were designated as an independent external test set to perform external validation and temporal validation on the AW-stacking model. The data set compiled from the literature included all requisite input features and output variables, resulting in a complete data set with no missing values. Outliers were identified and removed before model training. All input features and output variables were defined using standard SI units, and all mechanical property tests were conducted in accordance with the GB/T 17671-2021 standard. To ensure consistency, all flexural and *CS* data extracted from specimens of varying geometries were standardized to equivalent 40 mm × 40 mm × 160 mm strength values using the conversion factors reported in Ref. [8]. The data set contains three categorical (non-continuous) input features, including *XDP*, *W*, and *Mold*. One-hot encoding was employed to transform these data by creating new binary (0 or 1) feature columns for each category. To address the intra-study correlation inherent in data compiled from multiple literature sources and to prevent data leakage, a unique "group ID" was assigned to all samples originating from the same source. Consequently, group cross-validation (GCV) was strictly implemented using these group IDs

throughout all subsequent data set partitioning procedures. The final data set comprises a total of 858 sets of *CS* data and 442 sets of *FS* data. The statistical and categorical characteristics of the data set are listed in Table 1. Data density histograms for the flexural and *CS*s of MPC-UHPC were plotted to visually illustrate the distribution of the output variables, as shown in Fig. 2. The *FS* data points are primarily concentrated in the 10 to 25 MPa range, while the *CS* data points are mainly distributed within the 20 to 120 MPa range.

2.2 Data set analysis

During the modeling process, the Pearson correlation coefficient (PCC) was used to quantify the linear correlation between input features and output variables. A PCC value approaching ±1 signifies a stronger linear correlation between features [45]. A PCC analysis was conducted on the 14 input features and two output variables of the prediction model for the mechanical properties of MPC-UHPC prepared at negative temperatures. The calculation formula is presented in Eq. (1), and the results are shown in Fig. 3. As shown in Fig. 3, most of the features do not exhibit a significant linear correlation, as indicated by absolute PCC values below 0.5. The primary objective of this modeling was to investigate the influence of individual input features and the synergistic effects of multiple input features on the mechanical properties of MPC-UHPC prepared at negative temperatures. Consequently, the PCC value was not used as the sole criterion for feature selection, and the results of the analysis were regarded as a reference point. Although some input features show PCC values close to 0.7, such as the correlation between the *XDP* and *M*/*P*,

Table 1 Statistical and categorical characteristics of input features and output variables

Category	Variable	Type	Regular range/Category	Mean		Standard deviation		Standard error	
				FS	*CS*	*FS*	*CS*	*FS*	*CS*
Input	*T* (°C)	numerical	−30–20	13.25	5.90	14.08	17.04	0.67	0.59
	$M^{1)}/P$		0.8–5	3.07	3.35	1.03	1.01	0.05	0.04
	$W/C^{2)}$		0.1–0.2	0.15	0.15	0.03	0.02	0.01	0.01
	B/*M* (%)		2–15	6.46	6.26	2.50	2.92	0.12	0.10
	S/*B*		0–2	0.95	0.54	0.18	0.49	0.01	0.02
	LBM/*M* (%)		0–12	0.67	0.81	2.22	2.37	0.11	0.08
	FA (%)		0–30	4.1	2.49	6.59	5.44	0.31	0.19
	SF (%)		0–20	0.21	0.42	1.53	2.24	0.07	0.07
	V_f (%)		0–2.5	0.94	0.50	0.98	0.84	0.05	0.03
	Age (h)		1.5–3600	268.26	179.04	445.58	345.04	21.27	11.92
	L/*D*		30/50/65/85	–	–	–	–	–	–
	XDP	categorical	ADP (0)/PDP (1)	–	–	–	–	–	–
	W		Water (0)/Crushed ice (1)	–	–	–	–	–	–
	Mold		Plastic (0)/Steel (1)	–	–	–	–	–	–
Output	*FS* (MPa)	numerical	0.1–38.4	14.75	–	7.22	–	0.34	–
	CS (MPa)		0.18–158.3	–	53.83	–	36.67	–	1.27

Note: 1) $M = DBM + LBM$; 2) $C = M + XDP + B$.

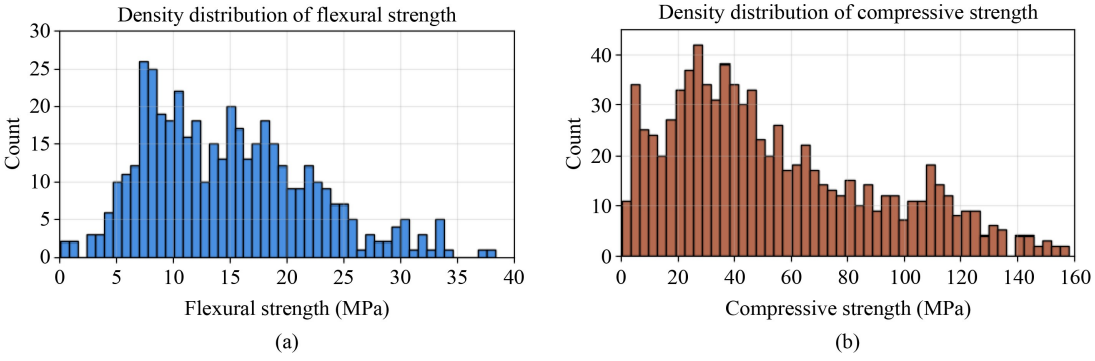

Fig. 2 Data distribution of the mechanical property of MPC-UHPC prepared at negative temperatures: (a) *FS*; (b) *CS*.

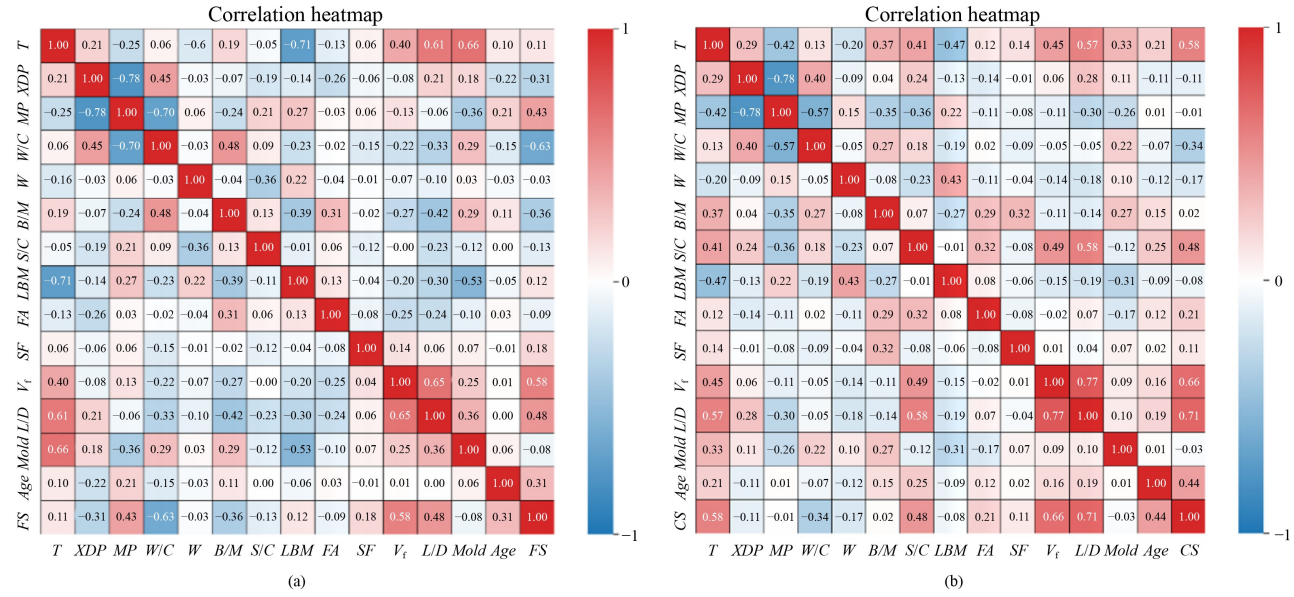

Fig. 3 PCC matrix of the features in the data set: (a) *FS*; (b) *CS*.

and between the V_f and L/D. These values remain within an acceptable range. Therefore, all 14 input features were retained for developing the prediction models.

$$PCC = \frac{\sum_{i=1}^{N}\left(X_i-\overline{X}\right)\left(Y_i-\overline{Y}\right)}{\sqrt{\sum_{i=1}^{N}\left(X_i-\overline{X}\right)^2}\sqrt{\sum_{i=1}^{N}\left(Y_i-\overline{Y}\right)^2}}, \quad (1)$$

where X_i and Y_i represent the sample values, $\overline{X}$ and $\overline{Y}$ are the sample mean values, and N is the sample size.

2.3 Data set evaluation

In this study, R^2, mean absolute error (*MAE*), *MSE*, and root mean squared error (*RMSE*) were used as evaluation metrics to select the base learners, determine the hyperparameter optimization algorithm, and assess the predictive accuracy of the models. An R^2 value approaching 1 indicates a superior model fit and improved explanatory ability for the data. *MAE*, *MSE*, and *RMSE* are used to measure the discrepancy between predicted and actual values. Regarding these metrics, values nearer to zero indicate superior predictive accuracy. The formulas for these metrics are provided in Eqs. (2)–(5).

$$R^2 = 1-\frac{\sum_{i=1}^{n}\left(Y_i-\hat{Y}_i\right)^2}{\sum_{i=1}^{n}\left(Y_i-\overline{Y}_i\right)^2}, \quad (2)$$

$$MAE = \frac{1}{n}\sum_{i=1}^{n}\left|Y_i-\hat{Y}_i\right|^2, \quad (3)$$

$$MSE = \frac{1}{n}\sum_{i=1}^{n}\left(\hat{Y}_i-Y_i\right)^2, \quad (4)$$

$$RMSE = \sqrt{\frac{1}{n}\sum_{i=1}^{n}\left(\hat{Y}_i-Y_i\right)^2}, \quad (5)$$

where Y_i is the actual values, $\hat{Y}_i$ and $\overline{Y}$ represent the predicted value and the mean of the predicted values, respectively, n is the sample size.

3 Methodology

3.1 Base machine learning models

The initial step in developing a high-accuracy AW-stacking model involved selecting the base learners. The ML algorithms considered in this study included ridge regression, LR, lasso regression (Lasso), elastic net regression (Enet), Bayesian linear regression (BR), SVR, decision tree regression (DR), adaptive boosting (AB), RF, XGB, CB, and light gradient boosting (LGB). Based on the comprehensive performance metrics of each base learner on both the training and testing data sets, RF, CB, XGB, and LGB were ultimately selected as the base learners for the AW-stacking model. The schematic diagrams of the four ML algorithms are shown in Fig. 4.

All four selected models are ensemble models. Of these, RF uses the bagging method, which involves constructing multiple decision trees with added randomness in both sample and feature selection, and then combining their outputs through voting or averaging [46]. In predicting the mechanical properties of MPC-UHPC prepared at negative temperatures in this study, RF effectively enhanced model stability and generalization

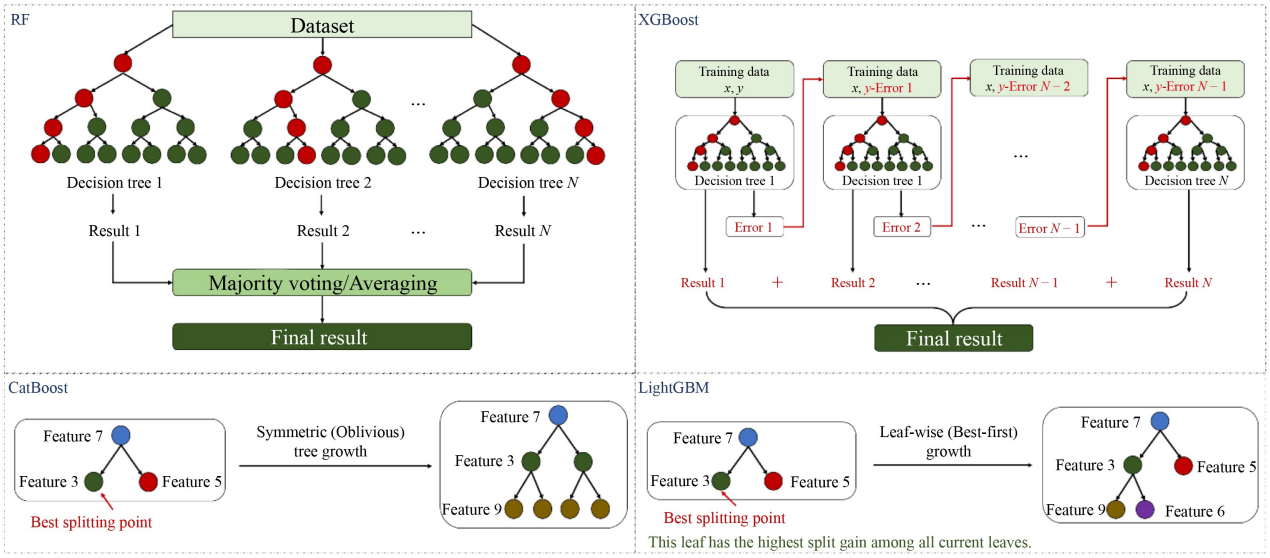

Fig. 4 Schematic diagrams of the base learner.

capabilities, thereby reducing the influence of occasional experimental errors on the final prediction results. The other three algorithms are improved variants of the GBDT algorithm. The fundamental methodology of XGB is characterized by its regularized objective function and its efficient optimization through second-order Taylor expansion. In this study, XGB effectively learned the variation trends in the mechanical properties of MPC-UHPC at negative temperatures based on input features such as T and M/P, even when using a limited number of data points. Furthermore, it enabled precise control of model complexity to prevent overfitting [47]. The advantage of CB resided in its ability to effectively learn from discrete categorical features, such as the type of phosphate or mold material, thereby enabling efficient and robust handling of categorical features while mitigating the risk of target leakage [48]. The notable training speed of LGB on large-scale data sets is primarily due to its implementation of two key techniques: gradient-based one-side sampling and exclusive feature bundling [49].

3.2 Tuning hyperparameter

Model hyperparameters influence the learning process, model complexity, and convergence rate, with various hyperparameter combinations resulting in significant differences in predictive performance. Consequently, the predictive accuracy can be substantially enhanced by reasonably assigning model hyperparameters. In this study, three optimization algorithms were employed, including adaptive grid search (AGS), enhanced grey wolf optimizer (EGWO), and Bayesian optimization (BO).

AGS improves optimization efficiency and reduces computational cost by dynamically adjusting the search focus and granularity throughout the iterative process. This facilitates a progressive transition from coarse-grained global exploration to fine-grained local refinement optimization [50]. The EGWO is a metaheuristic algorithm that simulates the population structure and hunting strategies of wolves. In this algorithm, the α, β, and δ wolves guide the population's position updates within the solution space to enhance its global search capability [51]. It does not depend on gradient information and requires minimal parameter setup, which improves its ability to achieve better global search performance in nonlinear, high-dimensional hyperparameter spaces. The BO constructs a surrogate model and an acquisition function to balance exploration of uncertain regions with the exploitation of currently optimal solutions, thereby approaching the global optimum with fewer training data and reduced computational costs [52].

3.3 Adaptive weighted stacking model

The stacking model uses a multi-level learning framework that enhances predictive accuracy through training on the combined prediction results of different base learners [53,54], as shown in Fig. 5. In the first layer, multiple base learners are trained in parallel. In the second layer, the prediction results from the first-layer base learners are combined and fed into a meta-learner for secondary training, after which regression determines the final prediction results. Nevertheless, the conventional stacking model typically employs an equal-weight averaging method to combine predictions from base learners. A notable limitation of this method is that the valuable predictive results obtained from high-accuracy models may be diminished by the error noise originating from models with lower accuracy.

An AW-stacking model was proposed to predict the mechanical properties of MPC-UHPC prepared at negative temperatures to avoid this problem. The complete model workflow is illustrated in Fig. 6.

To avoid any potential data leakage, all procedures related to model selection, hyperparameter tuning, and stacking weight calculation were carried out entirely within the training set, and no information from the test set was accessed at any stage of model development. The workflow of the AW-stacking model mainly includes the following.

1) The training set was split into five disjoint subsets, and a 5-fold GCV process was conducted for each base learner.

2) In each fold, the validation error ε_m^k was calculated according to Eq. (6), and the accuracy coefficient α_m^k of the mth base learner in the kth fold was calculated according to Eq. (7).

$$\varepsilon_m^k = \frac{1}{n_{\text{val}}^k} \sum_{i=1}^{n_{\text{val}}^k} (y_i - \hat{y}_i)^2, \tag{6}$$

where ε_m^k represents the *MSE* of the mth base learner in the kth fold, m is the number of base learners, n_{val}^k is the number of validation samples in the kth fold, y_i and $\hat{y}_i$ are the actual value and predicted value of the ith sample in the validation set, respectively.

$$\alpha_m^k = \frac{1}{\varepsilon_m^k + \delta}, \tag{7}$$

where α_m^k is the accuracy coefficient, δ is e^{-6} to avoid

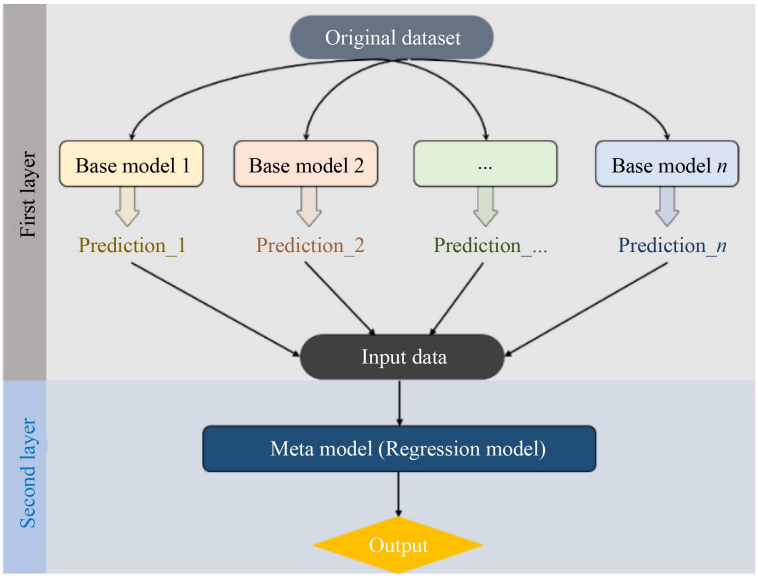

Fig. 5 Flowchart of stacking ensemble model.

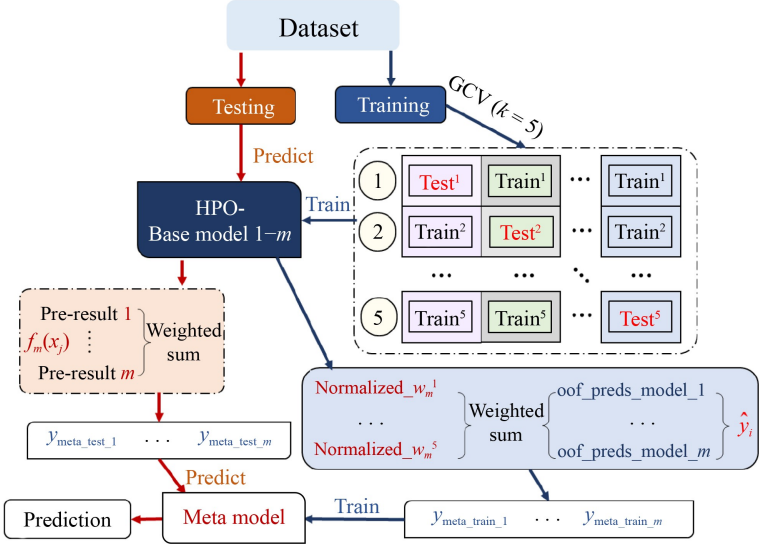

Fig. 6 Flowchart of the AW-stacking strategy.

division by zero.

3) The α_m^k were then normalized using the softmax function to obtain the w_m^k of each base learner in the kth fold, the calculation formula is Eq. (8).

$$w_m^k = \frac{\exp(\alpha_m^k)}{\sum \exp(\alpha_m^k)}, \tag{8}$$

where w_m^k represents the initial weight.

4) A smoothing mechanism was applied by performing a weighted fusion of the initial weight from the current fold with the weights from its adjacent folds ($k-1$ and $k+1$) to obtain the $smoothed\_w_m^k$ (Eq. (9)).

$$smoothed\_w_m^k = \beta \cdot w_m^k + \frac{1-\beta}{2}\left(w_m^{k-1} + w_m^{k+1}\right), \tag{9}$$

where $smoothed\_w_m^k$ represents the smoothed weight of the mth model on the kth fold, β is the smoothing coefficient, ranging from 0 to 1, w_m^{k-1} and w_m^{k+1} are the initial weights in the adjacent folds, respectively.

5) The $smoothed\_w_m^k$ were normalized to obtain $normalized\_w_m^k$ (Eq. (10)).

$$normalized\_w_m^k = \frac{smoothed\_w_m^k}{\sum smoothed\_w_m^k}, \tag{10}$$

where $normalized\_w_m^k$ is the final weight.

6) The meta-features were then constructed. A weighted sum of the $\hat{y}_i$, generated by each base learner during cross-validation was performed with $normalized\_w_m^k$ to obtain the $y_{\text{meta\_train}}$ (Eq. (11)), $y_{\text{meta\_test}}$ (Eq. (12)) was constructed by multiplying the $f_m(x_j)$ with the average weight of each model from the 5-fold GCV, and then summing the results.

$$y_{\text{meta\_train}} = \sum_{m=1}^{M}\sum_{k=1}^{5} normalized\_w_m^k \cdot \hat{y}_i, \tag{11}$$

$$y_{\text{meta\_test}} = \sum_{m=1}^{M}\left(\sum_{k=1}^{5} normalized\_w_m^k\right) \cdot f_m(x_j), \tag{12}$$

where $y_{\text{meta\_train}}$ and $y_{\text{meta\_test}}$ are the meta-feature data set for training and testing, $f_m(x_j)$ is the prediction value of sample x_j in the original testing set by the mth base learner.

7) Finally, Bayesian Ridge Regression was employed as the meta-learner. The meta-learner was trained on $y_{\text{meta\_train}}$ and tested on $y_{\text{meta\_test}}$, outputting the final prediction results.

Unlike the ordinary-stacking model, which integrates base learners using equal weights, the AW-stacking approach assigns weights according to the overall predictive performance of each base learner in GCV. When a base learner exhibits low validation error across the folds, it receives a higher accuracy coefficient, resulting in a larger final normalized weight; conversely, weaker-performing base learners are assigned lower weights. Because these weights are deterministically set by the fixed data set and the cross-validation structure, they remain constant after model training and do not adjust during the prediction phase. This performance-based weighting strategy effectively emphasizes the contribution of high-quality base learners and avoids the performance degradation associated with simple averaging, where all models contribute equally. As a result, the AW-stacking model achieves improved overall predictive accuracy and stability.

3.4 Shapley additive explanations-based model interpretability analysis

Although the AW-stacking model developed in this study showed high predictive accuracy, its complex internal structure and opaque decision-making process limited its interpretability. Used the SHAP analysis method to clarify the influence patterns and importance ranking of input features on the prediction models. Based on principles from cooperative game theory, this method fairly and accurately assigns the output results to each input feature, to quantify its contribution to the prediction process [55]. By combining the global feature importance bar plot and the summary plot, both the ranking of feature importance and the direction of feature influence were obtained. Furthermore, the SHAP dependence plot was employed to identify the nonlinear relationships between the mechanical properties of MPC-UHPC at negative temperatures and the input features.

4 Results and discussion

4.1 machine learning models selection

In this study, prediction models corresponding to 12 ML algorithms were developed, and their predictive performance was methodically assessed under default hyperparameter settings to evaluate their ability in predicting the mechanical properties of MPC-UHPC prepared at negative temperatures. To improve the reliability of the prediction models, the data set was split into a training set and a testing set (8:2 ratio). Additionally, a 5-fold GCV was performed on the training set, where the data set was randomly divided into five separate subsets. This procedure, which effectively controlled the risk of overfitting and enhanced the reliability of the prediction results, was consistently adopted in all subsequent analyses.

4.1.1 Predictive performance of machine learning models

The predictive performance of the 12 ML models for the

mechanical properties of MPC-UHPC prepared at negative temperatures was initially assessed using scatter plots, as shown in Figs. 7 and 8.

The proportion to which the data points approach the ideal diagonal line ($y = x$) directly reflects each model's predictive accuracy and generalization ability. The assessment of the models' performance was conducted by analyzing the proportion of data points within the error

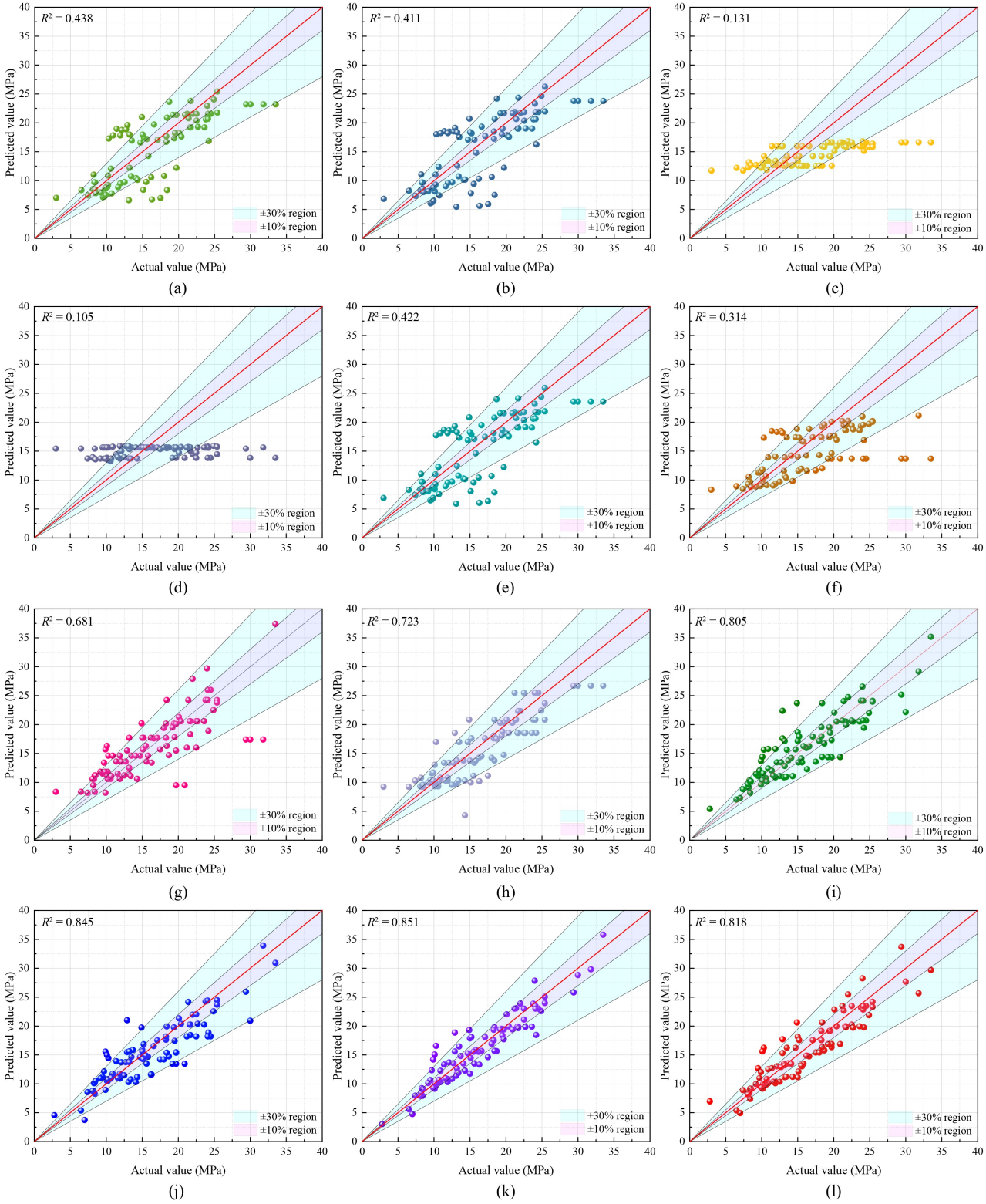

Fig. 7 Scatterplot of the actual and predicted values of MPC-UHPC *FS*: (a) Ridge; (b) LR; (c) Lasso; (d) Enet; (e) BR; (f) SVR; (g) DR; (h) AB; (i) RF; (j) XGB; (k) CB; (l) LGB.

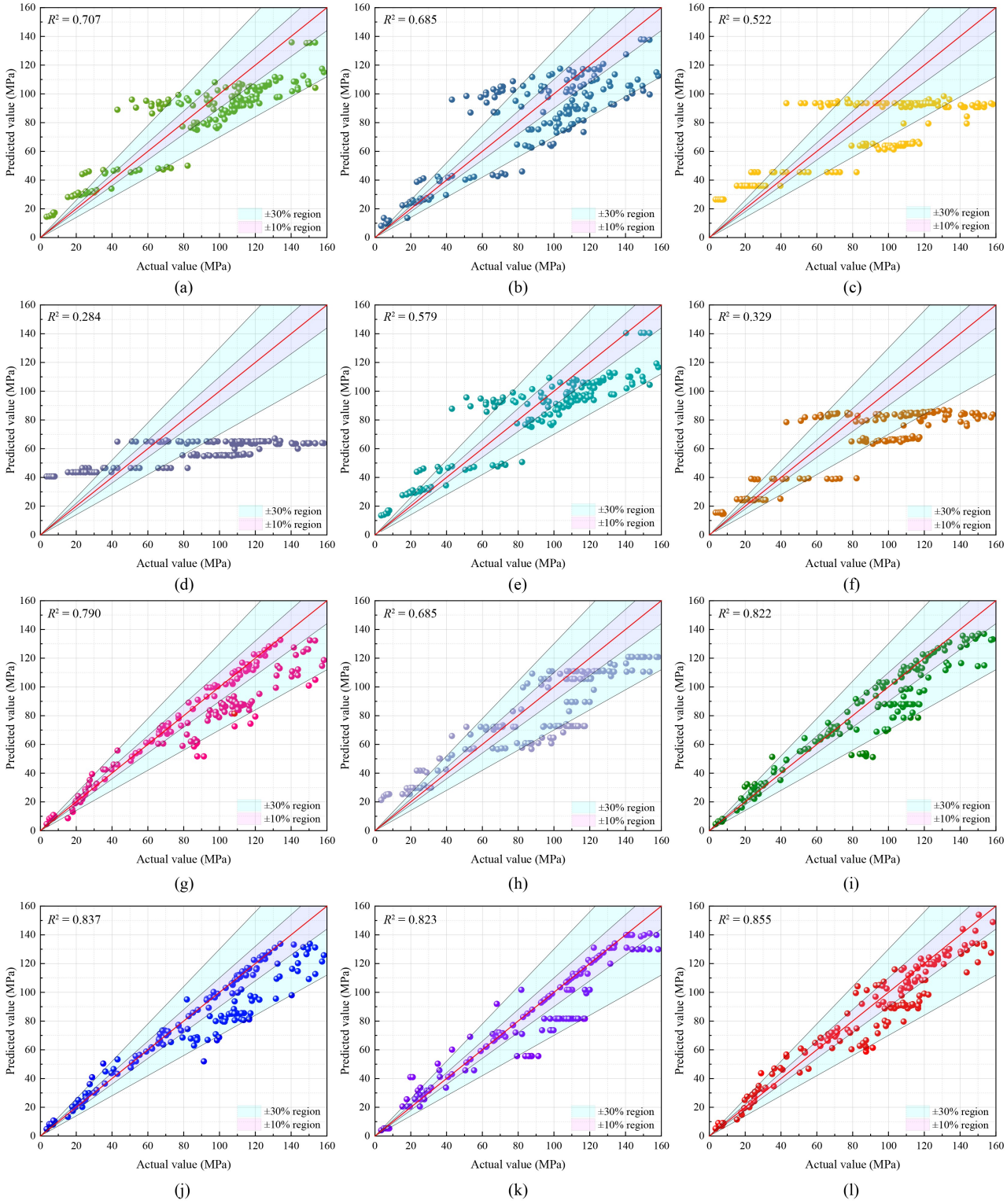

Fig. 8 Scatterplot of the actual and predicted values of MPC-UHPC *CS*: (a) Ridge; (b) LR; (c) Lasso; (d) Enet; (e) BR; (f) SVR; (g) DR; (h) AB; (i) RF; (j) XGB; (k) CB; (l) LGB.

area of ±10% and ±30%, with a higher percentage of data points within the ±10% range indicating superior predictive precision.

As shown in Fig. 7, notable differences are identified among the models in predicting the *FS* of MPC-UHPC prepared at negative temperatures. The Enet and SVR model performs worse, as most data points fall outside the ±30% error area. Linear models, including Ridge, LR, Lasso, Enet, and BR, also show poor performance because the data points are widely spread. Only about

50% of the data points are within the ±10% error area, indicating a tendency to overestimate low-strength data and underestimate high-strength data. This indicates that these models face challenges in accurately learning the intricate variation pattern of the *FS* of MPC-UHPC prepared at negative temperatures. The prediction results of the AB model show some improvement relative to the linear models. Overall, the prediction points generated by the DR, RF, XGB, CB, and LGB models are more densely concentrated within the ±30% error area, indicating that these models achieve better predictive accuracy.

According to Fig. 8, ensemble models including XGB, CB, LGB, and RF persistently exhibit superior performance in predicting the *CS* of MPC-UHPC prepared at negative temperatures, with the data points significantly concentrated within the ±30% error area. In contrast, SVR and linear models perform poorly with noticeable prediction errors. Based on the visualization of the prediction results, it is found that RF, XGB, CB, and LGB have greater advantages in learning the complex nonlinear relationships between the input features and the mechanical properties of MPC-UHPC prepared at negative temperatures.

4.1.2 Evaluation of machine learning prediction models

The predictive accuracy of the 12 ML models was quantitatively evaluated using R^2, *MAE*, *MSE*, and *RMSE* metrics. The evaluation results are listed in Table 2. As shown in Table 2, RF, XGB, CB, and LGB demonstrate significantly superior predictive accuracy on the testing set in comparison to the other models.

Among the four models, the CB model achieves the highest accuracy in predicting the *FS* of MPC-UHPC prepared at negative temperatures, with an R^2 of 0.851 and an *RMSE* of 2.25. The LGB model provides the most accurate *CS* predictions, with R^2 and *RMSE* values of 0.855 and 12.73, respectively. In contrast, the remaining models show limited predictive capacity, with R^2 values below 0.5 for *FS* and below 0.7 for *CS*. RF and XGB

Table 2 Performance analysis of 12 ML models for mechanical properties prediction

Algorithm	Prediction	R^2		*MAE*		*MSE*		*RMSE*	
		train	test	train	test	train	test	train	test
Ridge	*FS*	0.735	0.438	2.68	3.88	13.03	15.92	3.61	3.99
	CS	0.803	0.707	10.87	19.06	224.70	404.01	14.99	20.10
LR	*FS*	0.939	0.411	2.62	3.95	13.54	26.01	3.68	5.10
	CS	0.744	0.685	12.69	20.80	287.30	572.64	16.95	23.93
Lasso	*FS*	0.338	0.131	4.67	4.83	34.46	38.44	5.87	6.20
	CS	0.667	0.522	15.83	25.74	361.38	905.41	19.01	30.09
Enet	*FS*	0.209	0.105	5.22	5.11	41.60	47.33	6.45	6.88
	CS	0.429	0.284	21.95	33.13	727.92	2421.62	26.98	49.21
BR	*FS*	0.738	0.422	2.64	3.92	13.62	25.50	3.69	5.05
	CS	0.794	0.579	14.75	20.17	302.06	638.07	17.38	25.26
SVR	*FS*	0.697	0.314	2.79	4.09	15.76	30.36	3.97	5.51
	CS	0.581	0.329	17.28	30.56	511.66	1372.70	22.62	37.05
DR	*FS*	0.826	0.681	2.36	3.27	8.88	12.04	2.98	3.47
	CS	0.873	0.790	7.28	18.29	102.62	327.61	10.13	18.10
AB	*FS*	0.858	0.723	2.24	2.74	13.84	30.25	3.72	5.50
	CS	0.805	0.685	12.88	21.51	247.43	501.76	15.73	22.40
RF	*FS*	0.938	0.805	1.59	2.14	5.86	9.24	2.42	3.04
	CS	0.936	0.822	5.85	18.08	59.44	356.83	7.71	18.89
XGB	*FS*	0.983	0.845	1.39	1.62	3.84	4.62	1.96	2.15
	CS	0.941	0.837	4.71	14.97	37.45	283.59	6.12	16.84
CB	*FS*	0.962	0.851	1.45	1.78	1.82	5.06	1.35	2.25
	CS	0.927	0.823	5.14	17.13	47.47	331.97	6.89	18.22
LGB	*FS*	0.925	0.818	1.27	2.02	7.29	8.47	2.70	2.91
	CS	0.973	0.855	3.89	12.65	29.27	162.05	5.41	12.73

models still maintain acceptable accuracy, with R^2 values exceeding 0.8. Linear models and SVR show clear underfitting, as reflected by low R^2 values and higher *RMSE* values on the testing set. These quantitative metrics were entirely congruent with the qualitative results derived from the scatter plot analysis described earlier.

4.2 Hyperparameter tuning results

4.2.1 Optimization effectiveness of different algorithms

The hyperparameters of the four base learners were optimized using AGS, EGWO, and BO, and the results are listed in Tables 3–5. All three optimization methods collectively improved the model's predictive accuracy to varying degrees, with EGWO providing the most significant enhancement. During the optimization of the CB and LGB model, EGWO improved performance on the testing set, achieving R^2 values of 0.876 and 0.891 for *FS* and *CS*, respectively. Meanwhile, the *RMSE* values dropped to 1.80 and 8.27.

Compared with AGS, EGWO achieved an approximate 3.9% increase in R^2 and a reduction of over 20% in *RMSE* for mechanical property prediction of MPC-UHPC, demonstrating its higher accuracy and highlighting

Table 3 Performance metrics of EGWO-optimized models

Algorithm	Prediction	R^2		*MAE*		*MSE*		*RMSE*	
		train	test	train	test	train	test	train	test
EGWO-RF	*FS*	0.938	0.843	1.52	2.03	5.25	7.38	2.29	2.72
	CS	0.966	0.857	4.08	13.85	29.51	162.11	5.43	12.73
EGWO-XGB	*FS*	0.991	0.870	1.31	1.43	3.26	3.35	1.81	1.83
	CS	0.984	0.860	4.01	10.3	21.69	110.88	4.66	10.53
EGWO-CB	*FS*	0.973	0.876	1.19	1.45	1.28	3.25	1.13	1.80
	CS	0.958	0.873	4.27	12.92	23.90	125.55	4.89	11.20
EGWO-LGB	*FS*	0.938	0.857	1.12	1.81	4.41	5.75	2.10	2.40
	CS	0.993	0.891	2.41	8.60	11.92	68.49	3.45	8.27

Table 4 Performance metrics of BO-optimized models

Algorithm	Prediction	R^2		*MAE*		*MSE*		*RMSE*	
		train	test	train	test	train	test	train	test
BO-RF	*FS*	0.941	0.852	1.49	1.99	5.23	6.54	2.29	2.56
	CS	0.95	0.842	4.72	13.41	33.40	180.26	5.78	13.43
BO-XGB	*FS*	0.995	0.861	1.28	1.60	3.55	3.96	1.88	1.99
	CS	0.973	0.876	3.83	11.08	19.11	101.08	4.37	10.05
BO-CB	*FS*	0.975	0.860	1.43	1.61	1.15	4.72	1.07	2.17
	CS	0.956	0.852	4.91	14.71	29.21	198.39	5.40	14.09
BO-LGB	*FS*	0.931	0.846	1.20	1.89	5.29	6.77	2.30	2.60
	CS	0.989	0.879	2.91	10.00	15.08	93.56	3.88	9.67

Table 5 Performance metrics of AGS-optimized models

Algorithm	Prediction	R^2		*MAE*		*MSE*		*RMSE*	
		train	test	train	test	train	test	train	test
AGS-RF	*FS*	0.947	0.818	1.48	2.08	5.48	9.01	2.34	3.00
	CS	0.959	0.831	5.26	16.15	45.25	275.78	6.73	16.61
AGS-XGB	*FS*	0.98	0.85	1.40	1.50	3.80	4.23	1.95	2.06
	CS	0.979	0.843	4.52	12.72	30.4	171.22	5.51	13.09
AGS-CB	*FS*	0.969	0.853	1.38	1.69	1.72	5.06	1.31	2.24
	CS	0.939	0.837	5.00	16.80	36.1	256.62	6.01	16.02
AGS-LGB	*FS*	0.948	0.827	1.22	1.88	7.48	7.21	2.73	2.69
	CS	0.985	0.858	3.67	11.16	23.14	135.13	4.81	11.62

EGWO's excellent global search ability and efficient hyperparameter optimization in complex, high-dimensional, and nonlinear hyperparameter spaces.

4.2.2 Optimal hyperparameter values of base learners

The optimal hyperparameters of the four base learners for predicting the flexural and *CS*s of MPC-UHPC prepared at negative temperatures are listed in Table 6. All optimal hyperparameter values fell within a reasonable range. For example, the 'max_depth' required by the XGB model for *CS* prediction was 18, which significantly exceeded the value of 5 for *FS* prediction. This finding indicated that the XGB model leveraged deep tree structures to map the nonlinear dependencies between the input features and the mechanical properties of MPC-UHPC at negative temperatures. In the LGB model, the hyperparameter choices balanced model complexity with computational efficiency. For *CS* prediction, 'num_leaves' was set to 59 and 'max_depth' to 9. In contrast, for *FS*, these were adjusted to 38 and 14, indicating that the LGB model was capable of adaptively adjusting to the feature distributions of different output variables.

Table 6 Optimal hyperparameter values of base learners

ML model	Hyperparameter	Range	*FS* model value	*CS* model value
RF	n_estimators	[100, 2000]	1176	1032
	min_samples_split	[2, 20]	4	2
	min_samples_leaf	[1, 10]	2	1
	max_features	SQRT	10	8
	min_impurity_decrease	[0, 0.2]	0	0
XGB	n_estimators	[100, 2000]	615	972
	learning_rate	[0.01, 0.2]	0.13	0.17
	max_depth	[3, 20]	5	18
	min_child_weight	[1, 10]	1	3
	gamma	[0, 1]	0.25	0.72
	subsample	[0.5, 1]	0.83	0.71
	colsample_bytree	[0.5, 1]	0.70	0.83
	reg_alpha	[0, 1]	0.1	0.18
	reg_lambda	[0, 1]	0.05	0.42
CB	iterations	[500, 2000]	1435	1674
	learning_rate	[0.01, 0.2]	0.20	0.15
	depth	[4, 10]	8	9
	min_data_in_leaf	[1, 50]	17	26
	subsample	[0.5, 1]	0.81	0.92
	reg_lambda	[0, 1]	0.35	0.57
LGB	n_estimators	[100, 2000]	1654	1982
	learning_rate	[0.01, 0.2]	0.18	0.11
	num_leaves	[20, 100]	38	59
	max_depth	[3, 20]	14	9
	min_child_samples	[5, 50]	5	16
	subsample	[0.5, 1]	0.65	1.0
	colsample_bytree	[0.5, 1]	0.73	0.95
	reg_alpha	[0, 1]	0.42	0.36
	reg_lambda	[0, 1]	0.15	0.10

4.3 Predictive performance of the adaptive weighted stacking model

The comparison between the predicted and actual values of the AW-stacking model for the mechanical properties of MPC-UHPC at negative temperatures is shown in Fig. 9. The predicted and actual values of flexural and *CS* are consistent, with most data points distributed along the ideal diagonal line and the majority falling within the ±10% error area. Compared to the fitting results of the individual base learners shown in Figs. 7 and 8, the scatter points of the AW-stacking model are more concentrated, and there are fewer outliers, indicating better fitting ability and higher predictive accuracy.

The trend of prediction errors for the mechanical properties of MPC-UHPC at negative temperatures as a function of strength is shown in Fig. 10. It shows that although the magnitude of the model's error tends to increase with the strength level, the prediction errors for the *FS* of MPC-UHPC are largely controlled within a ±2.5 MPa range, demonstrating the good predictive accuracy. The accuracy of the AW-stacking model in predicting the *CS* of MPC-UHPC is further validated by Fig. 10(b). Despite involving a larger volume of data and a wider range of numerical fluctuations, the AW-stacking model still accurately predicts the variation trend of the actual *CS*. The majority of errors are controlled within ±10 MPa, with the positive and negative errors symmetrically distributed. This shows that the model maintains a stable predictive capability, even with multiple parameter inputs such as *T*, age, and *W*/*C*.

The comparison of predictive performance metrics for the stacking and AW-stacking models is listed in Table 7. Compared to the individual prediction models optimized by EGWO (Table 3), the stacking model for predicting MPC-UHPC *CS* shows an improvement in the R^2 value of the testing set, increasing from 0.891, which is achieved by the best-performing single model (LGB), to 0.908. After applying the adaptive weighted strategy, the R^2 value of the AW-stacking model further increases to 0.935, representing an improvement of approximately 3%. In addition, the RMSE decreases from its initial value of 8.27 to 6.42, a reduction of 22.4%. For *FS* prediction, the R^2 value of the AW-stacking model increases to 0.917, and the *RMSE* decreases by 20.56% compared with the best base model (EGWO-CB). Furthermore, the predictive performance of the AW-stacking model is validated using an external test set,

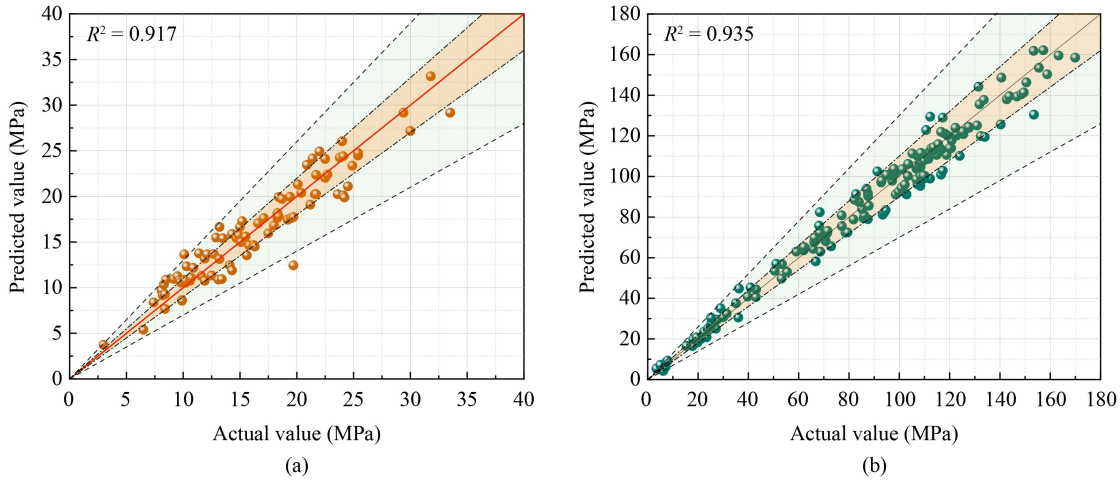

Fig. 9 Scatterplot of the AW-stacking model for predicting the mechanical property: (a) *FS*; (b) *CS*.

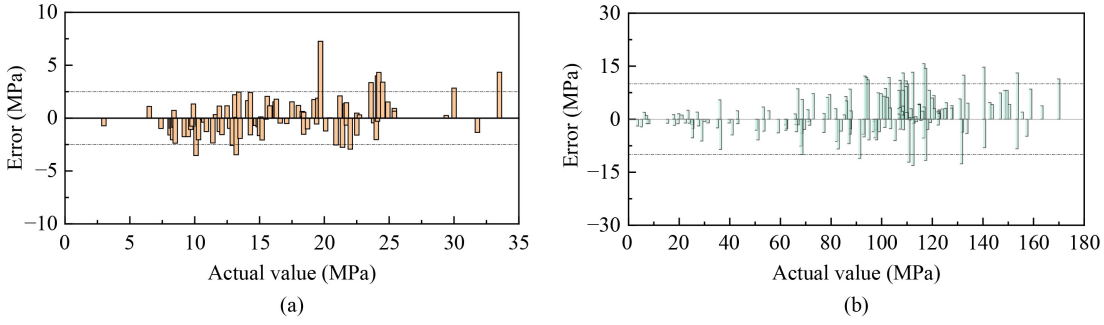

Fig. 10 Distribution of prediction residuals versus actual strength values for the mechanical properties of MPC-UHPC: (a) *FS*; (b) *CS*.

Table 7 Evaluation indexes of the Stacking model and the AW-stacking model

Evaluation index	Algorithm	Set	R^2	*MAE*	*MSE*	*RMSE*
FS	Stacking	test	0.886	1.30	2.84	1.68
	AW-stacking	test	0.917	1.18	2.06	1.43
		external test	0.904	1.23	2.46	1.57
CS	Stacking	test	0.908	8.01	57.84	7.61
	AW-stacking	test	0.935	5.23	41.26	6.42
		external test	0.922	7.06	48.22	6.94

achieving R^2 values of 0.904 and 0.922 in the prediction tasks for the flexural and *CS*s of MPC-UHPC prepared at negative temperatures, respectively. These results indicate that introducing an adaptive weighting mechanism to integrate the outputs of multiple base learners effectively overcomes the limitations of a single model, improves the model's generalization ability, and facilitates a more accurate prediction of the mechanical properties of MPC-UHPC prepared at negative temperatures.

4.4 Shapley additive explanations-based interpretability analysis of the adaptive weighted stacking model

4.4.1 Feature importance analysis

Figure 11 illustrates the ranked importance of the top ten input features affecting the flexural and *CS* of MPC-UHPC prepared at negative temperatures. The SHAP heatmap for the AW-stacking model is shown in Fig. 12. The scatter points, which are colored from blue to red, represent feature values from low to high, while the horizontal axis shows the feature's contribution to the prediction (SHAP value). The results show that the *FS* is predominantly influenced by V_f, age, *W*/*C*, *L*/*D*, *M*/*P*, and *B*/*M*, whereas the *CS* exhibits greater sensitivity to *T*, age, *W*/*C*, V_f, *B*/*M*, and *LBM*/*M*.

In the *FS* prediction model, the mean SHAP value of V_f is 2.904 (Fig. 11(a)). Figure 12(a) shows that a higher V_f is associated with a positive SHAP contribution, indicating that increasing V_f improves the *FS* of MPC-UHPC prepared at negative temperatures. Conversely, the *FS* decreases significantly in specimens with low or no

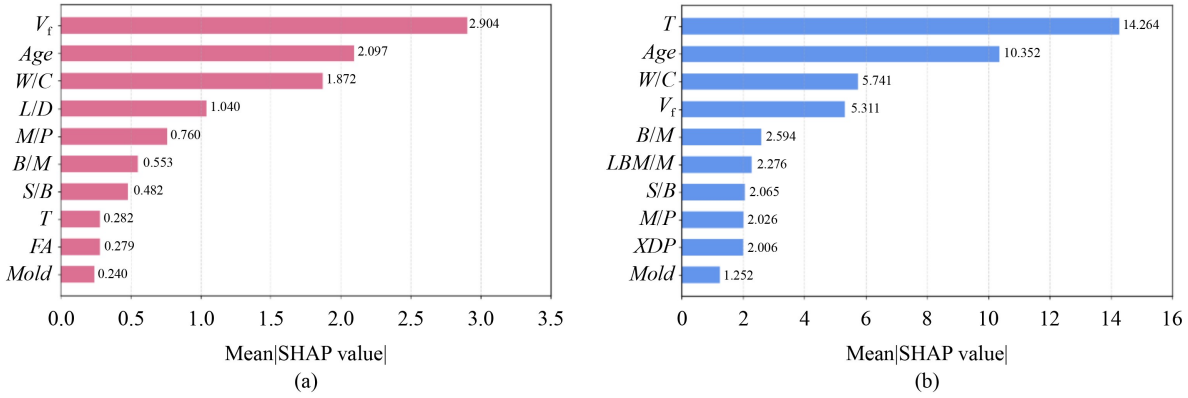

Fig. 11 Mean SHAP values of key input features: (a) *FS*; (b) *CS*.

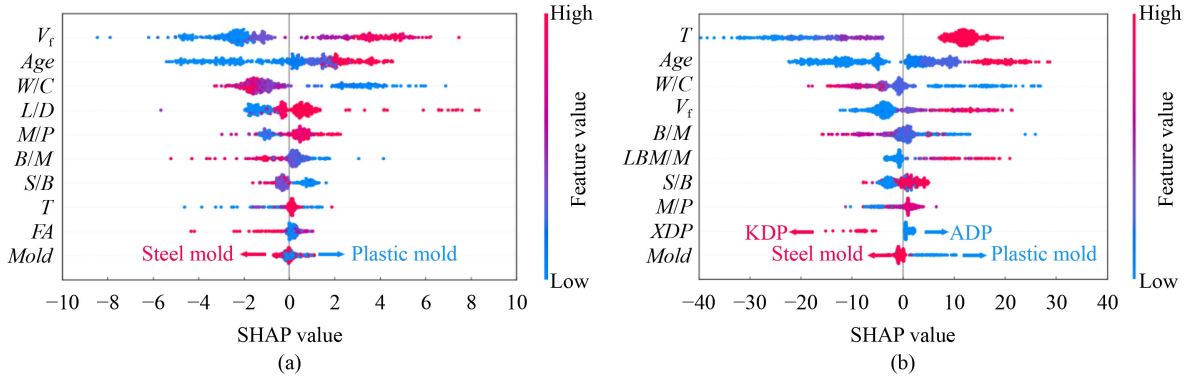

Fig. 12 Global SHAP heat map of key input features: (a) *FS*; (b) *CS*.

fiber volume fraction. Previous research indicated that adding 1.35% steel fibers at –20 °C increased the 28-d *FS* by about 34% and shifted the failure mode from brittle to ductile [8]. In contrast, the significance of V_f within the *CS* prediction model is lower than that of *T*, age, and *W*/*C*, thereby confirming that the fiber-bridging effect plays a comparatively limited role in enhancing *CS* MPC-UHPC [56]. Therefore, the V_f should be prioritized when designing for the *FS* of MPC-UHPC prepared at negative temperatures. In the *CS* prediction model, the mean SHAP value of *T* is 14.264 (Fig. 11(b)), confirming that *T* is the most important feature affecting the *CS* of MPC-UHPC at negative temperatures.

As shown in Figs. 11 and 12, the mechanical properties of MPC-UHPC prepared at negative temperatures are affected by both age and *W*/*C* together. Age positively correlates with SHAP values, indicating that longer curing age improves the mechanical properties of MPC-UHPC prepared at negative temperatures. Since the hydration reaction slows considerably at negative temperatures, extending the curing age is especially important for achieving optimal strength. A higher *W*/*C* corresponds to negative SHAP values, indicating that it has a negative impact on the development of mechanical properties. Similar conclusions were also reported by Luo et al. [57]. Besides the features mentioned earlier, the SHAP analysis shows that increasing the *B*/*M* ratio hampers the development of the mechanical properties of MPC-UHPC. Conversely, the additions of LBM appear comparatively advantageous, as reflected by its higher SHAP values. The results of the XDP indicate that the *CS* of the MgO–ADP system is superior to that of the MgO–KDP system. This phenomenon is attributed to the heat release from the MgO–ADP reaction being approximately twice as much as that of MgO–KDP, thereby enhancing the early hydration degree of MPC composites at negative temperatures [58]. Moreover, the hydration product of MgO–ADP, struvite, has an elastic modulus of about 42.40 GPa, which is significantly higher than that of K-struvite (37.3 GPa) [59,60]. Using plastic molds with low thermal conductivity (0.2 W/m·K), compared to steel molds with high conductivity (45 W/m·K), better slows heat dissipation. This reduces the adverse effects of low temperature on hydration heat release. Consequently, its feature points are associated with positive SHAP values, suggesting that casting MPC-UHPC with plastic molds at low temperatures can improve *CS*.

4.4.2 Dependency based on Shapley additive explanations analysis

To more directly examine the nonlinear relationship between individual input features and the mechanical properties of MPC-UHPC prepared at negative

temperatures, the six most influential input features were selected for single-feature analysis using SHAP dependence plots superimposed with global regression curves, as shown in Figs. 13 and 14.

The effects of V_f and L/D on the FS of MPC-UHPC are shown in Figs. 13(a) and 13(d), and both parameters show a positive correlation with FS. Steel fibers improve the FS of the matrix and reduce brittleness by bridging cracks and redistributing stresses [35,61,62]. Using steel fibers with a higher L/D ratio enhances their ability to bridge cracks, thereby increasing the post-cracking load capacity of the MPC-UHPC [63]. It is noteworthy that the

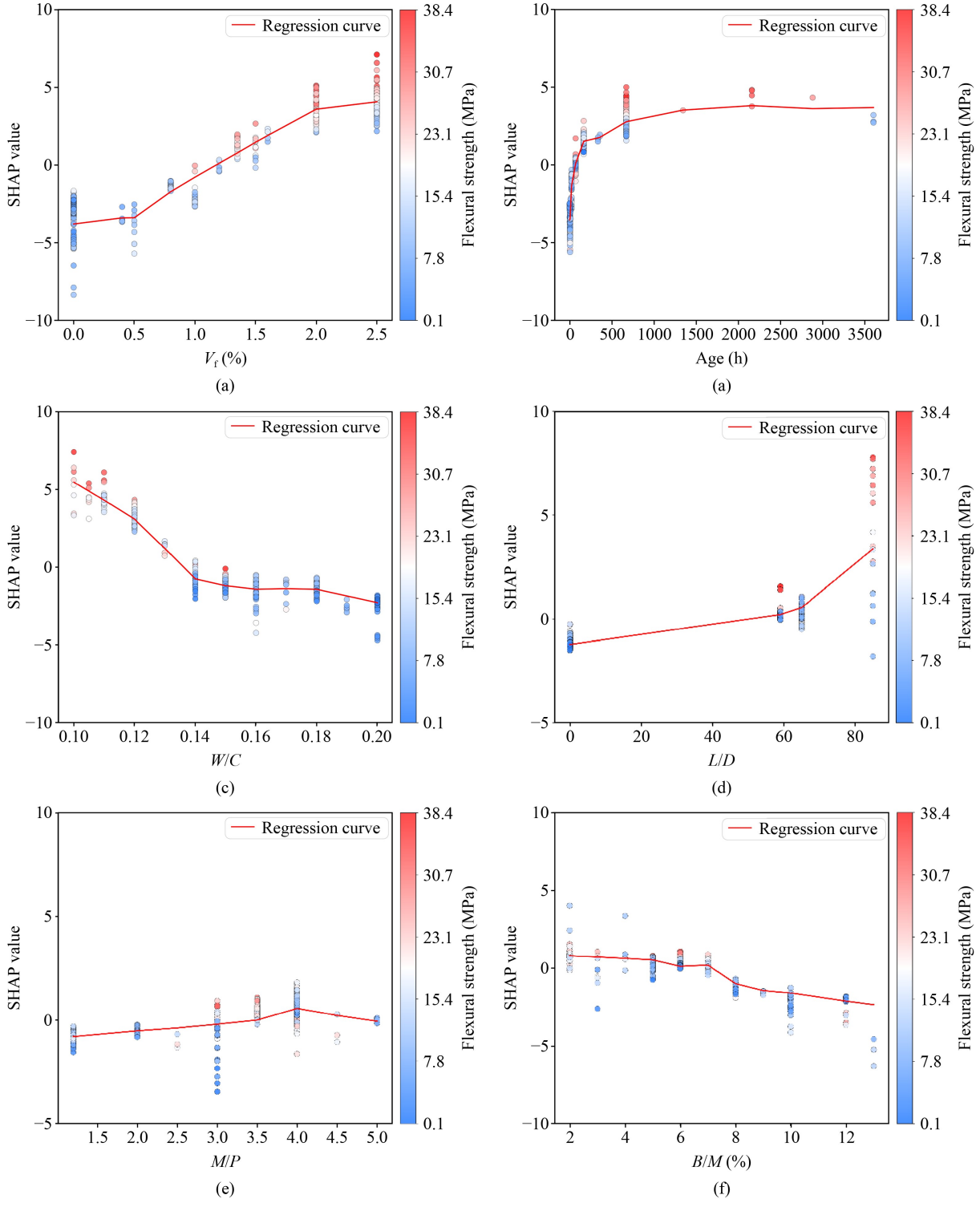

Fig. 13 Dependence of the top 6 input features on the FS of MPC-UHPC: (a) V_f; (b) age; (c) W/C; (d) L/D; (e) M/P; (f) B/M.

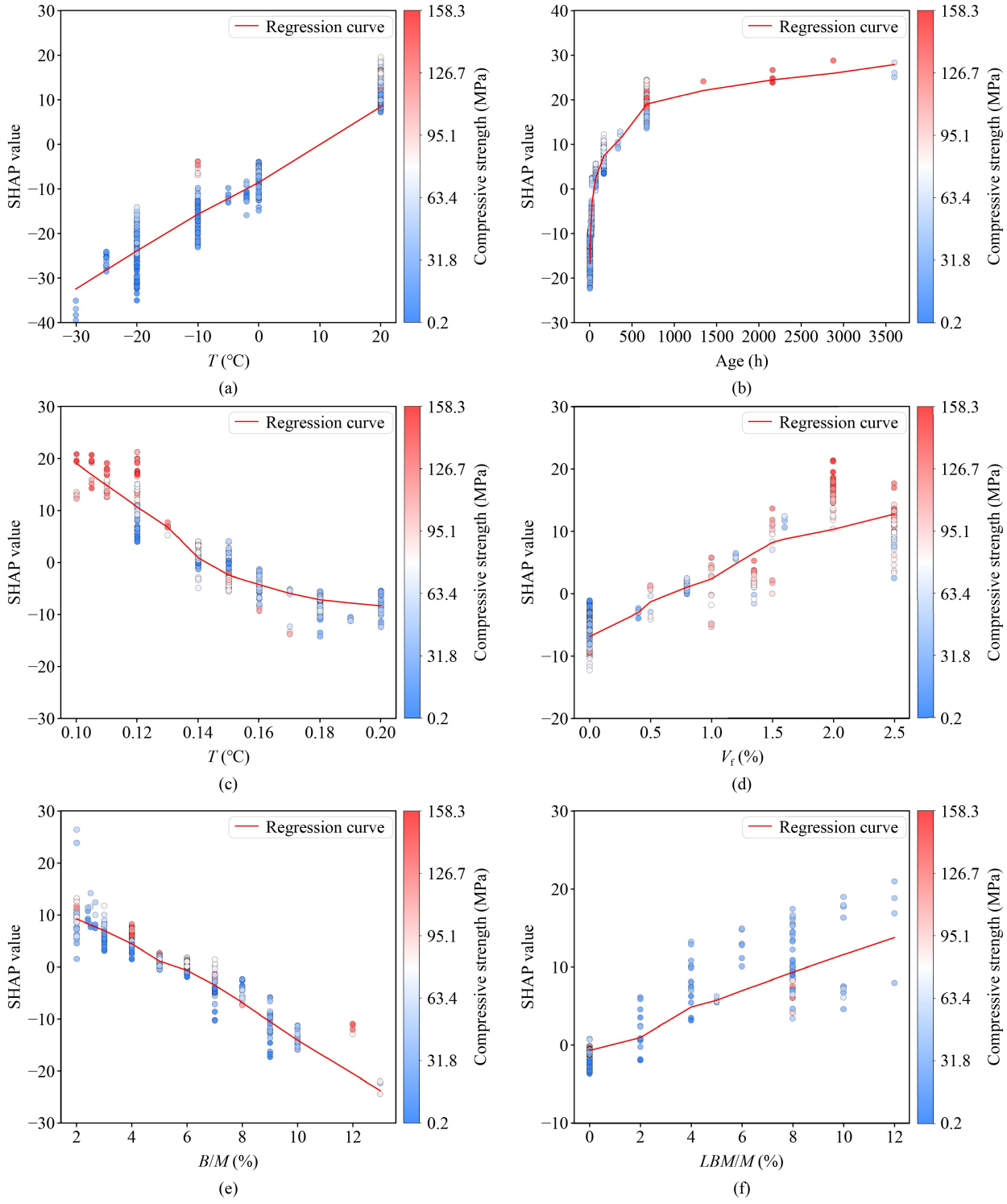

Fig. 14 Dependence of the top 6 input features on *CS* of MPC-UHPC: (a) *T*; (b) age; (c) *W*/*C*; (d) V_f; (e) *B*/*M*; (f) *LBM*/*M*.

FS increases quickly with V_f below 2.0%, but then tends to level off. This trend mainly results from the low *W*/*C* and high consistency of the MPC matrix, which necessitates longer mixing and vibration times to ensure uniform steel fiber dispersion at higher dosages. However, with a fixed *B*/*M*, the rapid-hardening characteristic of MPC results in insufficient time for adequate mixing. Consequently, when V_f exceeds 2%, the steel fibers are difficult to disperse uniformly, which manifests macroscopically as a decelerated rate of increase in *FS*.

The effect of the *M*/*P* on the *FS* is shown in Fig. 13(e), with the optimal range being 3.5 to 4.5. Within this range, residual MgO serves as a filler in the matrix, increasing

its density and thereby enhancing the *CS* [64]. An excessively low *M*/*P* ratio causes leftover phosphate in the reaction system, which may form defects [65,66]. Conversely, if the *M*/*P* ratio is excessively high, it results in inadequate struvite formation [67]. Both conditions decrease the matrix density, thereby deteriorating the mechanical properties of the MPC-UHPC.

As shown in Fig. 14(a), the *CS* has an approximately linear positive relationship with *T*. The MPC-UHPC reacts more fully at higher ambient temperatures, resulting in greater *CS*. However, *CS* development is significantly slower in severely cold environments (≤ –20 °C). As shown in Fig. 13(b), the SHAP value slowly turns negative as the ambient temperature drops. Low temperatures primarily inhibit MPC hydration by reducing struvite formation and the deterioration of its crystal morphology, which ultimately results in increased porosity and decreased *CS* [31]. The *CS* of MPC mortar was shown to be highly sensitive to ambient temperature, decreasing by approximately 30 MPa for each 10 °C drop, according to research by Yuan et al. [8]. Nevertheless, compared to ordinary Portland cement systems, where hydration nearly stops at sub-zero temperatures, MPC can continue to hydrate and gain strength below the freezing point [27].

Replacing a portion of DBM with LBM improves the *CS* of MPC-UHPC in cold environments, with the *CS* positively correlated to the LBM content (Fig. 14(f)). The rapid hydration heat released by LBM elevates the reaction system's initial temperature, which in turn accelerates the development of early *CS* in MPC-UHPC at low temperatures. Jia et al. [28] reported a remarkable 2.5-fold increase in the *CS* of MPC paste (from 18 to 45 MPa) when 12% LBM was added at –2 °C.

The combined effects of age, *W*/*C*, and *B*/*M* on the flexural and *CS*s of MPC-UHPC prepared at negative temperatures, with their corresponding SHAP dependence plots, are shown in Figs. 13(b), 13(c), 13(f), 14(b), 14(c), and 14(e). The mechanical properties of MPC-UHPC prepared at negative temperatures gradually improve with longer curing age. Based on the concrete's maturity theory [68,69], it can be inferred that a prolonged curing age can partially neutralize the retarding effects of low temperatures on MPC-UHPC hydration. A longer curing period allows more hydration products to form, which helps to cement unreacted DBM and residual inert materials, thereby gradually densifying the matrix structure and improving the mechanical properties. The mechanism by which *B*/*M* influences mechanical properties is similar to that of *T*, as an increased *B*/*M* or a decreased ambient temperature delays the hydration process. However, unlike the effect of low temperatures, which can be partly offset by increasing the curing age, the inhibitory impact of an excessive amount of retarder on the hydration is hard to eliminate entirely [70]. Therefore, B/M should be carefully controlled to avoid irreversible damage to the mechanical properties of MPC-UHPC, while ensuring workability. Lowering the *W*/*C* ratio is essential for enhancing the mechanical properties of MPC-UHPC. An excessively high *W*/*C* results in a large amount of free water that does not participate in hydration. When frozen, this free water causes defects and decreases the density of the matrix [62]. Therefore, the lowest *W*/*C* that still ensures acceptable workability should be chosen to achieve the optimal mechanical properties of MPC-UHPC at negative temperatures.

The influence patterns between input features and the mechanical properties, as shown by the SHAP analysis, were consistent with previous research results, confirming the high credibility of the AW-stacking prediction model. At the same time, the interpretability of SHAP should be understood within its valid range. The SHAP analysis only reflects the change regulation of input features learned by the model within the range covered by the data set (Table 1). When input values fall outside this effective range, for example, a curing temperature of 50 °C or a *W*/*C* approaching 0.50 lies beyond the conditions represented in the original data set, and the model cannot provide trustworthy strength predictions and the corresponding SHAP explanations under such scenarios.

4.5 Graphic user interface design

To assist non-specialist users in using the prediction model for the mechanical properties of MPC-UHPC, a GUI based on the Python/Qt framework was meticulously designed and implemented. The architecture of the prediction and analysis module is shown in Fig. 15, and a representative example of the user interface is provided in Fig. 16.

Figure 15 shows the Pre_UI layer, which creates a highly responsive and interactive interface using PyQt5 graphical components and layout strategies, enabling quick prediction and visualization of both compressive and *FS*s. The Pre_ML layer combines automated data processing, adaptive model tuning, and interpretability analysis, enabling one-click prediction of the mechanical properties. The data access object layer uses the singleton pattern to manage database connections and includes a least recently used cache for storing the three most recently accessed data sets.

In Fig. 16, after inputting the designated 14 parameters in the Mixing Proportions panel of the GUI, the user has the option to select either the system's default data set or a customized data set for model training. Furthermore, the user may freely choose among RF, XGB, CB, LGB, or the AW-stacking model to predict the mechanical properties of MPC-UHPC at negative temperatures. The selected algorithm is then automatically executed, and the predicted values of the negative-temperature mechanical properties of MPC-UHPC are ultimately provided.

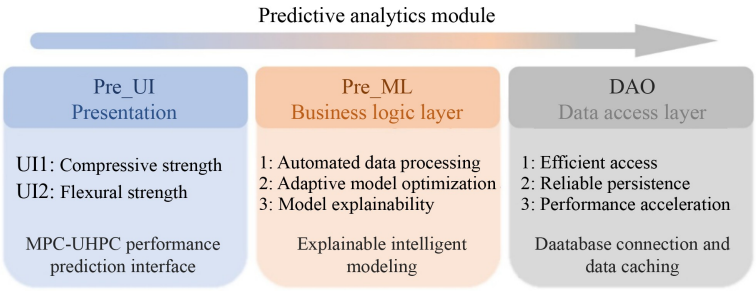

Fig. 15 System architecture of the predictive analytics module.

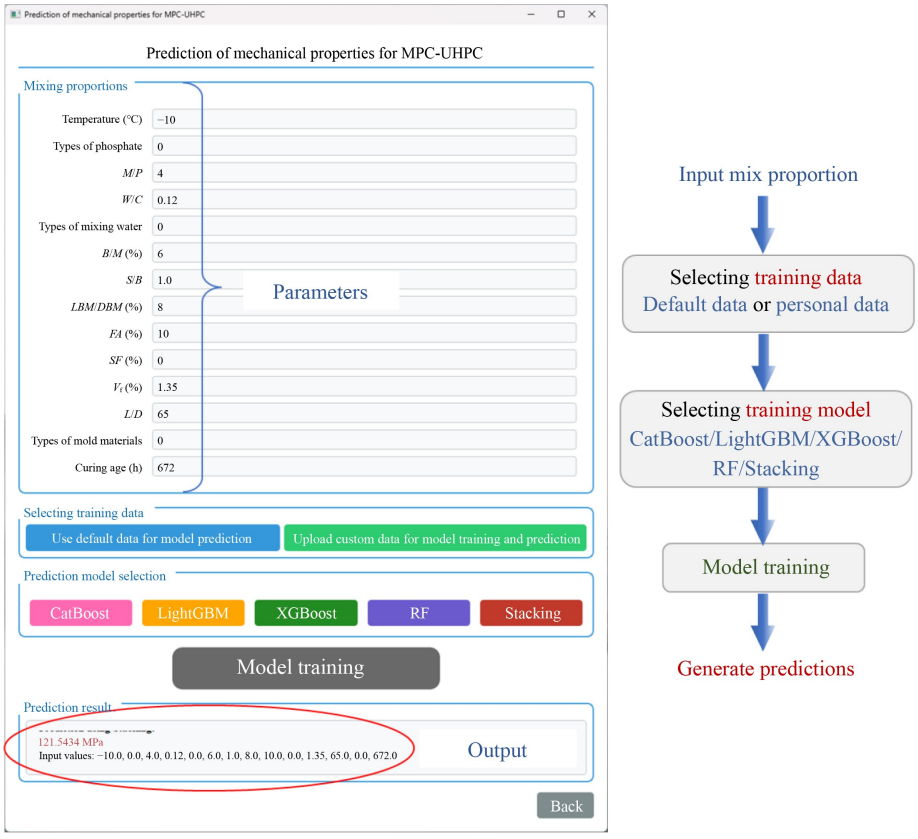

Fig. 16 GUI and workflow for AW-stacking model.

5 Conclusions and future perspectives

In this study, a database of MPC-UHPC mechanical properties prepared at negative temperatures was established based on publicly available literature. To ensure a robust and methodologically sound validation that prevents data leakage, a group ID was assigned to each literature source and strictly used in all GCV procedures. The EGWO was employed to optimize the hyperparameters of the base learners, and an AW-stacking model was constructed. This model achieved highly accurate predictions of MPC-UHPC mechanical properties at negative temperatures, with its generalization ability further confirmed using a completely unseen external test set. Finally, to better elucidate the relationship between key inputs and mechanical properties, the SHAP analysis method was utilized. The key conclusions can be summarized as.

1) Among 12 ML models, RF, XGB, CB, and LGB were identified as the optimal combination of base learners for predicting the MPC-UHPC mechanical properties at negative temperatures. The predictive accuracy and generalization ability of these four base learners were found to be superior to those of traditional linear models and the SVR model.

2) The AW-stacking model proposed in this study achieved highly accurate predictions for the mechanical properties of MPC-UHPC prepared at negative temperatures. The prediction coefficients of R^2 for flexural and *CS*s reached 0.917 and 0.935, respectively, while the *RMSE* decreased to 1.43 and 6.42. Compared with the most accurate base learner, EGWO-CB, the AW-stacking

model achieved further reductions of 20.6% and 22.4% in the *RMSE* for flexural and *CS* predictions, respectively, thus enhancing the overall predictive accuracy for the mechanical properties of MPC-UHPC.

3) SHAP global feature importance analysis indicated that T was the primary determinant of *CS* at negative temperatures, whereas V_f constituted the dominant factor for *FS* under identical conditions. Both mechanical properties were significantly influenced by age, with which they were positively correlated; similarly, the W/C exerted a substantial negative effect on mechanical properties.

4) The SHAP analysis provides critical insights into the complex balance inherent in the design of MPC-UHPC mixtures. It indicates that while adopting the lowest possible W/C and B/M ratios, increasing V_f, and replacing DBM with LBM are key strategies for achieving superior mechanical properties at negative temperatures. But these strength-focused adjustments must be balanced against the practical constraint of ensuring reasonable fresh-state properties. Furthermore, the curing time of MPC-UHPC should be appropriately extended as the ambient temperature decreases.

Despite the AW-stacking model's success in predicting the hardened-state mechanical properties of MPC-UHPC at negative temperatures, its limitations in the context of practical engineering must be clearly stated. The AW-stacking model does not predict critical fresh-state properties, including workability, setting time, or pumpability, nor does it assess long-term durability metrics like frost resistance or shrinkage. Furthermore, the error margins tend to increase when predicting very high-strength values, which is linked to data scarcity in that range. A key focus of future research will be to incorporate these critical, multi-dimensional performance metrics into the database to develop a more comprehensive, multi-objective prediction framework.

Appendix

Table A1 Summary of data sources

Ref.	Published year	Research variable	Data volume	Temperature range (°C)
[3]	2020	*CS*	27	−20–20
[4]	2025	*FS*/ *CS*	8/8	−5–20
[31, 43]	2025/2023	*FS*/ *CS*	12/12	20
[5]	2022	*FS*/ *CS*	10/13	20
[6]	2024	*FS*/ *CS*	20/18	20
[7]	2024	*FS*/ *CS*	12/12	20
[8, 30]	2024/2022	*FS*/ *CS*	46/59	−30–20
[27, 42]	2019/2020	*CS*	46	−20–20
[28]	2021	*CS*	200	−20–20
[29, 41]	2022/2022	*CS*	33/70	−25–20
[32]	2018	*CS*	19	20
[33]	2024	*FS*/ *CS*	15/15	20
[34]	2023	*FS*/ *CS*	14/14	−20–20
[35]	2018	*FS*/ *CS*	72/75	20
[36]	2023	*CS*	40	20
[37]	2022	*FS*/ *CS*	42/42	0–20
[38]	2021	*FS*/ *CS*	36/36	20
[39]	2021	*FS*/ *CS*	122/122	20
[40]	2021	*CS*	12	−20–20
[44]	2024	*CS*	18	−30–20

Competing interests The authors declare that they have no competing interests.

References

1. Liu J, Wei J, Li J, Su Y, Wu C. A comprehensive review of ultra-high performance concrete (UHPC) behaviour under blast loads. Cement and Concrete Composites, 2024, 148: 105449
2. Fang B D, Hu Z J, Shi T, Liu Y, Wang X, Yang D, Zhu K, Zhao X, Zhao Z. Research progress on the properties and applications of magnesium phosphate cement. Ceramics International, 2023, 49(3): 4001–4016
3. Jia X, Luo J, Zhang W, Qian J, Li J, Wang P, Tang M. Preparation and application of self-curing magnesium phosphate cement concrete with high early strength in severe cold environments.

Materials, 2020, 13(23): 5587
4. Yuan J, Zhang Z, Chen X, Huang X, Cui A. Long-term performance of magnesium phosphate cement concrete prepared in the winter. European Journal of Environmental and Civil Engineering, 2025, 29(1): 176–200
5. Qin J, Dai F, Ma H, Dai X, Li Z, Jia X, Qian J. Development and characterization of magnesium phosphate cement based ultra-high performance concrete. Composites. Part B, Engineering, 2022, 234: 109694
6. Qin J, Zhang Z, Ma H, Dai X, Cheng X, Jia X, Qian J. Improving mechanical properties of magnesium phosphate cement-based ultra-high performance concrete by ultrafine fly ash incorporation. Construction and Building Materials, 2024, 448: 138198
7. He Z, Jiang Y, Shi J, Qin J, Liu D, Yalçınkaya Ç, He Y. Effect of silica fume on the performance of high-early-strength UHPC prepared with magnesium ammonium phosphate cement. Case Studies in Construction Materials, 2024, 20: e03351
8. Yuan J, Huang X, Chen X, Zhang Z, Ge Q, Liu Y. Potentialities of magnesium phosphate cement-based ultra-high-performance concrete in extremely cold weather construction. Construction and Building Materials, 2024, 456: 139297
9. Hou D, Chen D, Wang X, Wu D, Ma H, Hu X, Zhang Y, Wang P, Yu R. RSM-based modelling and optimization of magnesium phosphate cement-based rapid-repair materials. Construction and Building Materials, 2020, 263: 120190
10. Chou J, Tsai C. Concrete compressive strength analysis using a combined classification and regression technique. Automation in Construction, 2012, 24: 52–60
11. Yang J, Zeng B, Ni Z, Fan Y, Hang Z, Wang Y, Feng C, Yang J. Comparison of traditional and automated machine learning approaches in predicting the compressive strength of graphene oxide/cement composites. Construction and Building Materials, 2023, 394: 132179
12. Han T, Bhat R, Ponduru S A, Sarkar A, Huang J, Sant G, Ma H, Neithalath N, Kumar A. Deep learning to predict the hydration and performance of fly ash-containing cementitious binders. Cement and Concrete Research, 2023, 165: 107093
13. Sadrossadat E, Basarir H, Karrech A, Elchalakani M. Multi-objective mixture design and optimisation of steel fiber reinforced UHPC using machine learning algorithms and metaheuristics. Engineering with Computers, 2022, 38(S3): 2569–2582
14. Yu Y, Li W, Li J, Nguyen T N. A novel optimised self-learning method for compressive strength prediction of high performance concrete. Construction and Building Materials, 2018, 184: 229–247
15. Ghafari E, Bandarabadi M, Costa H, Júlio E. Prediction of fresh and hardened state properties of UHPC: comparative study of statistical mixture design and an artificial neural network model. Journal of Materials in Civil Engineering, 2015, 27(11): 04015017
16. Ben Chaabene W, Flah M, Nehdi M L. Machine learning prediction of mechanical properties of concrete: critical review. Construction and Building Materials, 2020, 260: 119889
17. Erdal H I. Two-level and hybrid ensembles of decision trees for high performance concrete compressive strength prediction. Engineering Applications of Artificial Intelligence, 2013, 26(7): 1689–1697
18. Nunez I, Marani A, Flah M, Nehdi M L. Estimating compressive strength of modern concrete mixtures using computational intelligence: A systematic review. Construction and Building Materials, 2021, 310: 125279
19. Asif U, Javed M F, Abuhussain M, Ali M, Khan W A, Mohamed A. Predicting the mechanical properties of plastic concrete: An optimization method by using genetic programming and ensemble learners. Case Studies in Construction Materials, 2024, 20: e03135
20. Khan A Q, Muhammad S G, Raza A, Chaimahawan P, Pimanmas A. Advanced machine learning techniques for predicting compressive strength of ultra-high performance concrete. Frontiers of Structural and Civil Engineering, 2025, 19(4): 503–523
21. Ma S, Gu J, Wang J, Shao Y, Zhang Z, Liu X. In-depth insight into the driving factors of the compressive strength development of MKPC based on interpretable machine learning methods. Journal of Industrial and Engineering Chemistry, 2025, 141: 305–318
22. Zhang J, Li T, Yao Y, Hu X, Zuo Y, Du H, Yang J. Optimization of mix proportion and strength prediction of magnesium phosphate cement-based composites based on machine learning. Construction and Building Materials, 2024, 411: 134738
23. Li Q, Song Z. Prediction of compressive strength of rice husk ash concrete based on stacking ensemble learning model. Journal of Cleaner Production, 2023, 382: 135279
24. Cui S, Yin Y, Wang D, Li Z, Wang Y. A stacking-based ensemble learning method for earthquake casualty prediction. Applied Soft Computing, 2021, 101: 107038
25. Li Q, Wang X. Bayesian optimization of stacking ensemble learning model for HPC compressive strength prediction. Expert Systems with Applications, 2025, 288: 128281
26. Huang X, Liu G, Zheng Y, Luo H. The performance of magnesium phosphate cement in negative temperature environment: A state-of-the-art review. Journal of Building Engineering, 2023, 76: 107278
27. Jia X, Li J, Wang P, Qian J, Tang M. Preparation and mechanical properties of magnesium phosphate cement for rapid construction repair in ice and snow. Construction and Building Materials, 2019, 229: 116927
28. Jia X, Luo J, Zhang W, Tang M, Qian J, Wang P, Li J. Reaction characteristics and compressive strength of magnesia-phosphate cement at negative temperatures. Construction and Building Materials, 2021, 305: 124819
29. Yuan J, Zhang Z, Chen X, Pan Z, Huang X. Early-aged mechanical properties of magnesium phosphate cement mixed with ice water in severe cold. Concrete, 2022, 2022(8): 10–14
30. Yuan J, Huang X, Chen X, Ge Q, Zhang Z. Early-age mechanical properties and hydration degrees of magnesium phosphate cement paste in freezing winter of cold regions. Construction and Building Materials, 2022, 345: 128337
31. Yuan J, Zhang Z, Chen X, Huang X. Microstructures and properties of modified magnesium phosphate cement mortar prepared at low temperatures and subjected to freeze-thaw cycling at early ages. Journal of Wuhan University of Technology. Materials Science Edition, 2025, 40(2): 427–438
32. Feng H, Sheikh M N, Hadi M N S, Feng L, Gao D, Zhao J. Interface bond performance of steel fibre embedded in magnesium phosphate cementitious composite. Construction and Building Materials, 2018, 185: 648–660

33. Chen X, Liu W, Cui A Q, Zheng H, Huang X, Yang W, Ge Y. Mechanical properties and freeze-thaw cycling resistance of magnesium phosphate cement mortar prepared at low temperatures in highland regions. Materials Reports, 2024, 38(17): 53–61
34. Li M, Yue Y, Qian J, Li Z, Tang M. Strength properties of low temperature magnesium phosphate cement concrete. Journal of Civil and Environmental Engineering, 2023, 45(2): 194–202
35. Feng H, Sheikh M N, Hadi M N S, Gao D, Zhao J. Mechanical properties of micro-steel fibre reinforced magnesium potassium phosphate cement composite. Construction and Building Materials, 2018, 185: 423–435
36. Dong D, Huang Y, Pei Y, Zhang X, Cui N, Zhao P, Hou P, Lu L. Effect of spherical silica fume and fly ash on the rheological property, fluidity, setting time, compressive strength, water resistance and drying shrinkage of magnesium ammonium phosphate cement. Journal of Building Engineering, 2023, 63: 105484
37. Liu J X, Yuan M, Hai R, Yang F, Zhang J, Li A. Investigation of the mechanical physical properties of fly ash modified magnesium phosphate cement repair mortar cured at varying temperatures. Buildings, 2022, 13(1): 88
38. Qin J H. Study on preparation and mechanical behavior of ultra-high strength magnesium phosphate cement composites. Dissertation for the Doctoral Degree. Chongqing: Chongqing University, 2019 (in Chinese)
39. Tang M. The Preparation and properties of ultra-high performance magnesium phosphate cement bridge deck pavement material. Thesis for the Master's Degree. Chongqing: Chongqing University, 2021 (in Chinese)
40. Ge Q. Hydration and pore structure of magnesium phosphate cement in natural environment of severe cold. Thesis for the Master's Degree. Harbin: Harbin Institute of Technology, 2021 (in Chinese)
41. Zhang Z. Property of magnesium phosphate cement-based materials mixed with ice and water in severe cold environment. Thesis for the Master's Degree. Harbin: Harbin Institute of Technology, 2022 (in Chinese)
42. Li J M. Preparation and mechanical properties of magnesium phosphate cement concrete for rapid repair construction in severe cold environment. Thesis for the Master's Degree. Chongqing: Chongqing University, 2020 (in Chinese)
43. Zhang Z. Effect of early freezing-thawing on late performance of magnesium phosphate cement-based material prepared at negative temperature. Thesis for the Master's Degree. Harbin: Harbin Institute of Technology, 2023 (in Chinese)
44. Xie J, Jin L Y, Li W, Zhang Y. Mechanical properties of steel fiber reinforced magnesium phosphate cement composites under negative temperature curing condition. Journal of Acta Materiae Compositae Sinica, 2024, 42(11): 6553 (in Chinese)
45. Gong H, Li Y, Zhang J, Zhang B, Wang X. A new filter feature selection algorithm for classification task by ensembling pearson correlation coefficient and mutual information. Engineering Applications of Artificial Intelligence, 2024, 131: 107865
46. Yoo S, Kim S J, Kim S J, Kang B B. AI-HydRa: Advanced hybrid approach using random forest and deep learning for malware classification. Information Sciences, 2021, 546: 420–435
47. Duan J, Asteris P G, Nguyen H, Bui X, Moayedi H. A novel artificial intelligence technique to predict compressive strength of recycled aggregate concrete using ICA-XGBoost model. Engineering with Computers, 2021, 37(4): 3329–3346
48. Zhang Y, Ren W, Lei J, Sun L C, Mi Y, Chen Y. Predicting the compressive strength of high-performance concrete via the DR-CatBoost model. Case Studies in Construction Materials, 2024, 21: e03990
49. Chun P J, Izumi S, Yamane T. Automatic detection method of cracks from concrete surface imagery using two-step light gradient boosting machine. Computer-Aided Civil and Infrastructure Engineering, 2021, 36(1): 61–72
50. Verwaeren J, Van der Weeën P, De Baets B. A search grid for parameter optimization as a byproduct of model sensitivity analysis. Applied Mathematics and Computation, 2015, 261: 8–27
51. Philip S, Marakkath N. Compressive strength prediction and feature analysis for GGBS-based geopolymer concrete using optimized XGBoost and SHAP: A comparative study of optimization algorithms and experimental validation. Journal of Building Engineering, 2025, 108: 112879
52. Hosseini Sarcheshmeh A, Etemadfard H, Najmoddin A, Ghalehnovi M. Hyperparameters' role in machine learning algorithm for modeling of compressive strength of recycled aggregate concrete. Innovative Infrastructure Solutions, 2024, 9(6): 212
53. Hamed A K, Elshaarawy M K, Alsaadawi M M. Stacked-based machine learning to predict the uniaxial compressive strength of concrete materials. Computers & Structures, 2025, 308: 107644
54. Shafighfard T, Kazemi F, Asgarkhani N, Yoo D Y. Machine-learning methods for estimating compressive strength of high-performance alkali-activated concrete. Engineering Applications of Artificial Intelligence, 2024, 136: 109053
55. Luo X, Li Y, Lin H, Li H, Shen J, Pan B, Bi W, Zhang W. Research on predicting compressive strength of magnesium silicate hydrate cement based on machine learning. Construction and Building Materials, 2023, 406: 133412
56. Ke S, Gao Z. Experimental and numerical study on flexural behavior of steel fiber reinforced high-strength concrete (SFRHC) beams. Scientific Reports, 2025, 15(1): 18338
57. Luo X, Li Y, Wang Q A, Mu J, Liu Y. Machine learning based modeling for predicting the compressive strength of solid waste material-incorporated magnesium phosphate cement. Journal of Cleaner Production, 2024, 442: 141172
58. Fan S, Chen B. Experimental study of phosphate salts influencing properties of magnesium phosphate cement. Construction and Building Materials, 2014, 65: 480–486
59. Li Y, Zhang G, Wang Z, Guan Z. Experimental-computational approach to investigate compressive strength of magnesium phosphate cement with nanoindentation and finite element analysis. Construction and Building Materials, 2018, 190: 414–426
60. Wang X, Hu X, Chong L, Yang J, Shi C. Effects of the combination of $NH_4H_2PO_4$ and KH_2PO_4 on the interfacial bond between magnesium phosphate cement and steel fiber. Construction and Building Materials, 2023, 407: 133405
61. Feng H, Shao Q, Yao X, Li L, Yuan C. Investigating the hybrid effect of micro-steel fibres and polypropylene fibre-reinforced

magnesium phosphate cement mortar. International Journal of Concrete Structures and Materials, 2022, 16(1): 35

62. Feng H, Chen G, Gao D, Zhao K, Zhang C. Mechanical properties of steel fiber-reinforced magnesium phosphate cement mortar. Advances in Civil Engineering, 2018, 2018(1): 3978318
63. Wang Z, Wu J, Wang J. Experimental and numerical analysis on effect of fibre aspect ratio on mechanical properties of SRFC. Construction and Building Materials, 2010, 24(4): 559–565
64. Wang A, Yuan Z, Zhang J, Liu L, Li J, Liu Z. Effect of raw material ratios on the compressive strength of magnesium potassium phosphate chemically bonded ceramics. Materials Science and Engineering C, 2013, 33(8): 5058–5063
65. Le Rouzic M, Chaussadent T, Stefan L, Saillio M. On the influence of Mg/P ratio on the properties and durability of magnesium potassium phosphate cement pastes. Cement and Concrete Research, 2017, 96: 27–41
66. Li Y, Sun J, Chen B. Experimental study of magnesia and M/P ratio influencing properties of magnesium phosphate cement. Construction and Building Materials, 2014, 65: 177–183
67. Wang A, Fan X, Li J, Chen D. Curing behavior and structure of magnesium phosphate chemically bonded ceramics with different MgO to KH_2PO_4 ratios. International Journal of Applied Ceramic Technology, 2015, 12(6): 1124–1130
68. Saul A G A. Principles underlying the steam curing of concrete at atmospheric pressure. Magazine of Concrete Research, 1951, 2(6): 127–140
69. Nurse R W. Steam curing of concrete. Magazine of Concrete Research, 1949, 1(2): 79–88
70. Dong J, Zheng W, Chang C, Wen J, Xiao X. Function and effect of borax on magnesium phosphate cement prepared by magnesium slag after salt lake lithium extraction. Construction and Building Materials, 2023, 366: 130280